

Fluidized bed coupled rotary reactor for nanoparticles coating via atomic layer deposition

Chen-Long Duan, Xiao Liu, Bin Shan, and Rong Chen

Citation: [Review of Scientific Instruments](#) **86**, 075101 (2015); doi: 10.1063/1.4926349

View online: <http://dx.doi.org/10.1063/1.4926349>

View Table of Contents: <http://scitation.aip.org/content/aip/journal/rsi/86/7?ver=pdfcov>

Published by the [AIP Publishing](#)

Articles you may be interested in

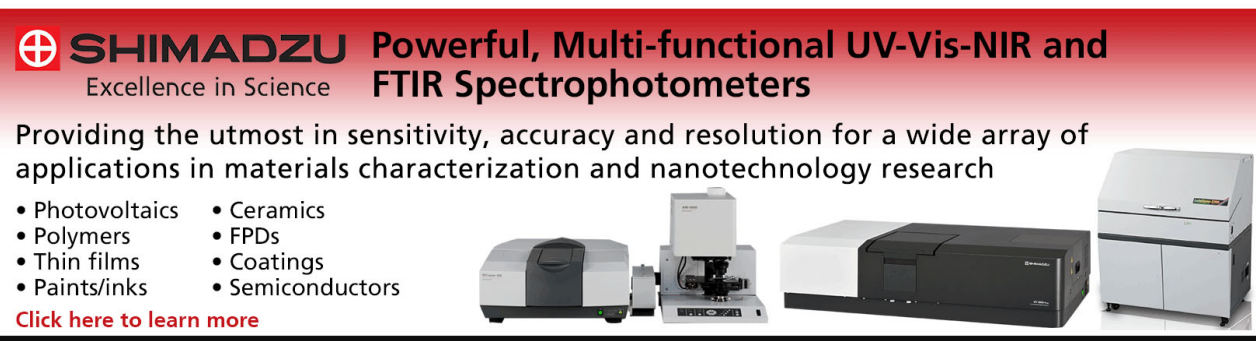
[Growth of crystalline Al₂O₃ via thermal atomic layer deposition: Nanomaterial phase stabilization](#)
APL Mat. **2**, 032105 (2014); 10.1063/1.4868300

[Reactor concepts for atomic layer deposition on agitated particles: A review](#)
J. Vac. Sci. Technol. A **32**, 010802 (2014); 10.1116/1.4851676

[Fluidized-bed atomic layer deposition reactor for the synthesis of core-shell nanoparticles](#)
Rev. Sci. Instrum. **85**, 013905 (2014); 10.1063/1.4863099

[Ultra-thin atomic-layer deposited alumina incorporating silica sol makes ultra-durable antireflection coatings](#)
J. Appl. Phys. **112**, 093517 (2012); 10.1063/1.4764332

[Rotary reactor for atomic layer deposition on large quantities of nanoparticles](#)
J. Vac. Sci. Technol. A **25**, 67 (2007); 10.1116/1.2393299




SHIMADZU Excellence in Science **Powerful, Multi-functional UV-Vis-NIR and FTIR Spectrophotometers**

Providing the utmost in sensitivity, accuracy and resolution for a wide array of applications in materials characterization and nanotechnology research

- Photovoltaics
- Polymers
- Thin films
- Paints/inks
- Ceramics
- FPDs
- Coatings
- Semiconductors

[Click here to learn more](#)



Fluidized bed coupled rotary reactor for nanoparticles coating via atomic layer deposition

Chen-Long Duan,¹ Xiao Liu,¹ Bin Shan,^{2,a)} and Rong Chen^{1,a)}

¹State Key Laboratory of Digital Manufacturing Equipment and Technology, School of Mechanical Science and Engineering, Huazhong University of Science and Technology, 1037 Luoyu Road, Wuhan, Hubei 430074, People's Republic of China

²State Key Laboratory of Material Processing and Die & Mould Technology, School of Materials Science and Engineering, Huazhong University of Science and Technology, 1037 Luoyu Road, Wuhan, Hubei 430074, People's Republic of China

(Received 13 May 2015; accepted 24 June 2015; published online 10 July 2015)

A fluidized bed coupled rotary reactor has been designed for coating on nanoparticles (NPs) via atomic layer deposition. It consists of five major parts: reaction chamber, dosing and fluidizing section, pumping section, rotary manipulator components, as well as a double-layer cartridge for the storage of particles. In the deposition procedure, continuous fluidization of particles enlarges and homogenizes the void fraction in the particle bed, while rotation enhances the gas-solid interactions to stabilize fluidization. The particle cartridge presented here enables both the fluidization and rotation acting on the particle bed, demonstrated by the analysis of pressure drop. Moreover, enlarged interstitials and intense gas–solid contact under sufficient fluidizing velocity and proper rotation speed facilitate the precursor delivery throughout the particle bed and consequently provide a fast coating process. The cartridge can ensure precursors flowing through the particle bed exclusively to achieve high utilization without static exposure operation. By optimizing superficial gas velocities and rotation speeds, minimum pulse time for complete coating has been shortened in experiment, and *in situ* mass spectrometry showed the precursor usage can reach 90%. Inductively coupled plasma-optical emission spectroscopy results suggested a saturated growth of nanoscale Al₂O₃ films on spherical SiO₂ NPs. Finally, the uniformity and composition of the shells were characterized by high angle annular dark field-transmission electron microscopy and energy dispersive X-ray spectroscopy. © 2015 AIP Publishing LLC. [<http://dx.doi.org/10.1063/1.4926349>]

I. INTRODUCTION

Nanoparticles (NPs) with large specific surface area have attracted much attentions in many fields, such as functional ceramics,¹ catalytic materials,^{2–4} magnetic recording medium,⁵ optical detection substrates,⁶ fuel cells,^{7,8} and biomedicines.^{9,10} Obtaining the desired chemical, electrical, biological, or thermal properties for these applications usually requires surface modifications. So far, several approaches have been developed for particle surface modifications. Among these approaches, solution-based synthesis has been widely used, but it suffers residual surfactants in the coatings and the film thickness control is complicated.^{11–14} As a gas phase surface modification method, atomic layer deposition (ALD) is quite attractive for its precise thickness control or even monolayer modifications with good conformity and uniformity.^{15–17} In a typical ALD cycle, different precursors are pulsed alternatively into reaction chamber, while surplus reactants and by-products are removed in intervals by a purge step of inert gas.¹⁸ Thickness of the film can be precisely controlled by the number of deposition cycles.

The challenge for particle surface modification using ALD is the large surface area and the nonuniform interstitials

in the particle bed, which demand special reactors and processes. In most commercial ALD reactors, particles are typically contained in a crucible and precursors diffuse through the interstitials in the fixed particle bed. Though these reactors have been used extensively, they still require extremely long time to ensure complete growth since it is difficult for precursors to diffuse deep inside the particle bed, as the studies reported by McCormick and Longrie *et al.*^{19,20} Another common way is supporting the particles by stainless steel or tungsten grids while precursors driven by a vacuum pump flow across the grids to react with reactive surface sites.^{21,22} Due to the fast flow rate, precursors usually tend to go through the channels in the particle bed, leading to some unreacted precursors being pumped out. To facilitate the precursors delivery to the particle surfaces, fluidized bed reactor (FBR) has been complemented by George and Wank *et al.* on many applications with different designs.^{3,4,23–31} The FBR disperses particles continuously, and its intense solid recirculation and constant gas–solid contact make the ALD coating more efficient. However, with the size of NPs decreasing, their interparticle cohesive forces are often much greater than the drag force exerted by the fluid. In this case, gas channels or slugs would occur through which some unreacted precursors would leave the particle bed directly.^{33–37} To improve the precursor utilization, Weimer and Detavernier groups developed rotary reactors where particles were lifted up by a low-speed rotating cartridge and fell off the wall

^{a)}Authors to whom correspondence should be addressed. Electronic addresses: rongchen@mail.hust.edu.cn and bshan@mail.hust.edu.cn

during coating. Within a precursor pulse period, the valve on the outlet was closed to expose particle surfaces to precursor gas adequately. However, cycle time was prolonged to obtain effective exposure of each particle, due to the lack of fast delivery of precursors.^{19,20,22,23,32}

In this paper, a rotary reactor coupled with fluidization is designed to improve the uniformity and efficiency of ALD on NPs. A double layer particle cartridge is utilized to enable particle fluidization and high speed rotation to overcome the cohesive forces of NPs and enhance gas-solid interactions. Pressure drop monitoring and its power spectrum density (PSD) analysis show the stability of fluidization. Furthermore, the enlarged bed void fraction and enhanced gas-solid interactions facilitate the transport of precursors throughout the particle bed. Precursors are forced to exclusively flow through the particle bed to obtain high precursor utilization. Microscopic characterizations validated the uniformity of Al₂O₃ films coated on spherical SiO₂ NPs. Conformal coatings on CeO₂ nanopolyhedra further revealed the generosity of the reactor on various nanostructures.

II. EXPERIMENT CONFIGURATION

As shown in Fig. 1, the reactor introduced in this work has five major parts: (A) the reaction chamber, (B) the dosing and fluidizing section, (C) the rotary particle cartridge, (D) the rotary manipulator components, and (E) the pumping section.

A. Reaction chamber

Fig. 2 presents a 3D diagram of the main reaction chamber, showing its assembling relationship with other sections. The reaction chamber is constructed from a 100 mm diameter and 250 mm long stainless steel tube. A standard 40 mm Conflat flange is welded on one end of the tube to interface

with rotary manipulator components. The cavity cover is installed to the other side of the tube by ISO-NW100 flange coordination. Four 16 mm Conflat flange ports are welded on the cylindrical surface of the tube. The first port is reserved for an Edwards Vacuum® pressure transducer, and the second one connects a Kurt J. Lesker® thermocouple feedthrough to detect chamber temperature. The left two ports are symmetrically distributed on the main tube, which connect dosing and fluidizing pipes. A clamshell style heater is fixed on the tube with insulation, while heat tapes are wrapped around the other exposed surfaces of chamber, benefiting uniform temperature distribution and less condensation of reactants on chamber walls. The chamber temperature is controlled by a single-phase AC voltage regulator and optimized by proportional integral differential (PID) parameters. Pressure drop is captured by readings from calibrated pressure transducers mounted on the main chamber and the outlet on the pumping bypass.

B. Dosing and fluidizing section

Precursors are pulsed into the reaction chamber separately to avoid CVD reactions inside the delivery pipes which are made from Swagelok® 1/4 in. stainless steel tubes and compression fittings. MKS® 1485 A mass flow controllers accurately adjust the flows of fluidizing gas and precursors. In order to obtain a continuous precursor flow, N₂ is injected into precursor bottles to carry precursors into the chamber.³⁸ Sequential selection of dosing was automatically controlled by a series of Swagelok® pneumatically activated diaphragm valves. Needle valves jointed to the precursor bottles are used to adjust precursor pulses. All the section is warmed by resistive tapes to prevent condensation and promote vapor pressure of solid precursor sources. Flexible coating recipe, including pressure drop, furnace temperature, rotation speed, and precursor dosing, is achieved by programmable logic

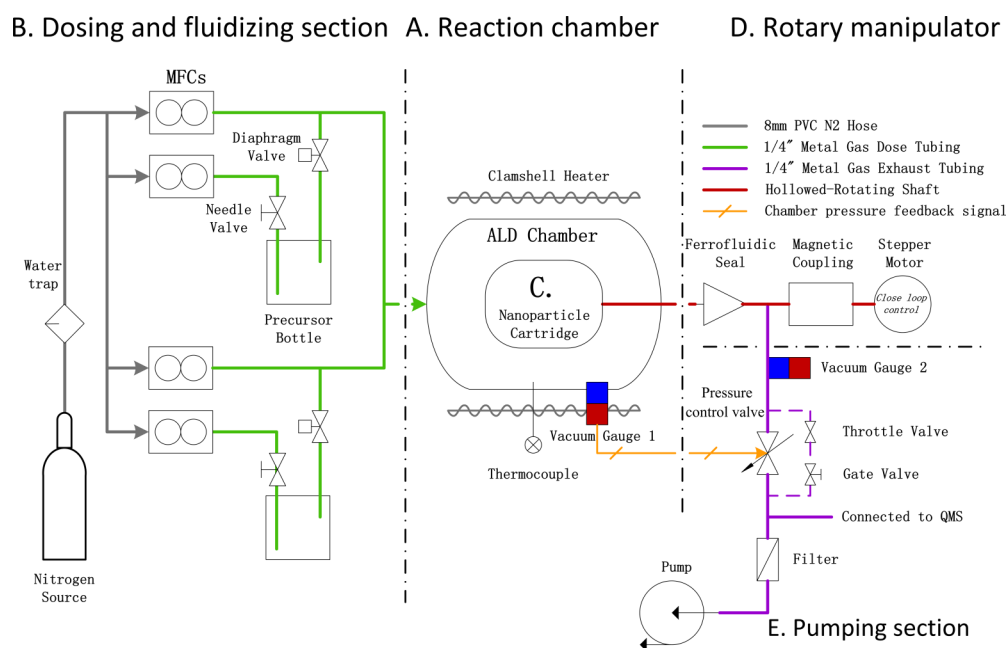


FIG. 1. Schematic diagram of fluidization coupled rotary reactor. The reactor consists of 5 sections: (A) the reaction chamber, (B) dosing and fluidizing section, (C) the rotary particle cartridge, (D) the rotary manipulator components, and (E) the pumping section.

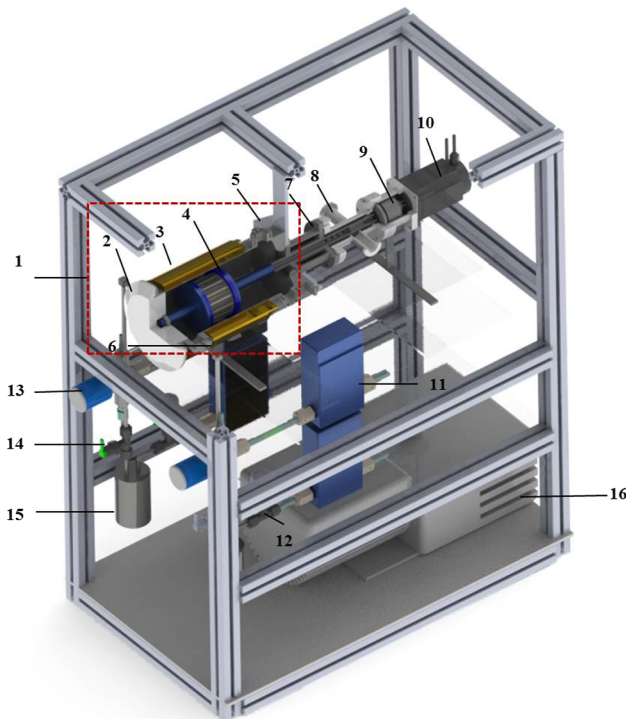


FIG. 2. 3D models of fluidization coupled rotary ALD reactor: (1) reaction chamber, (2) cavity cover, (3) heater, (4) nanoparticle cartridge, (5) vacuum gauge and thermocouple feedthrough connections, (6) precursor inlets, (7) magnetic fluid rotary feedthrough, (8) cross flange, (9) magnetic coupling, (10) stepper motor, (11) mass flow controller, (12) pneumatic valve, (13) ALD diaphragm valve, (14) needle valve, (15) precursor bottle, and (16) vacuum pump with a tube furnace and a filter (concealed in the picture).

controller and user interface written by LabVIEW. Real-time monitored data, such as pressure and rotation speed, are saved for follow-up analysis.

C. Nanoparticle cartridge

A rotary particle cartridge is designed to hold the particles during ALD reactions. Instead of stirring or vibrating in common ALD-FBR, this cartridge facilitates gas–solid interactions by centrifugal force during fluidization. The precursor diffusion depends not only on ALD kinetics but also on the gas throughput Q through the particle bed. So it would be beneficial to enlarge the gas throughput which correlates to the precursor diffusion. In the viscous regime, Equation (1) shows that the gas throughput Q is determined by the gas distribution area A , the gas conductance per area C_T , and pressure drop ΔP across the particle bed. Here, C_T is determined by the thickness of the particle bed, the gas viscosity, the pressure on the two sides of the bed, and the interstitial diameter which is involved with particle properties and fluidizing velocity. Given a certain amount of particles, larger gas distribution area A will decrease the bed thickness and then increase C_T . In addition, ΔP in a rotating fluidized particle bed is equal to its apparent weight and is in proportion to the square of rotation speed ω as Equation (2) shows, which can be much larger than that of conventional FBR. Here, r_0 and r_i are the radii of the cartridge and particle bed surface, ρ_p is particle density, ρ_f is fluidizing gas density, and ε is the void fraction in the particle

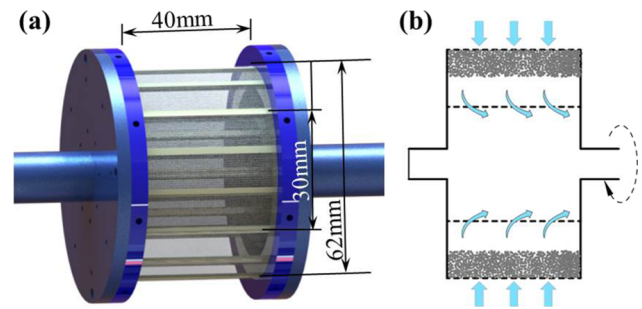


FIG. 3. (a) Simplified assembly drawing of particle cartridge and (b) schematic diagram of the particle cartridge.

bed. Therefore, the total gas throughput Q can be enlarged by increasing gas distribution area A and pressure drop ΔP , which could be implemented in designs by using the lateral surface of the cartridge as distributor and the rotation of the cartridge,

$$Q = AC_T\Delta P, \quad (1)$$

$$\Delta P = \int_{r_i}^{r_0} (1 - \varepsilon)(\rho_p - \rho_f)\omega^2 r dr. \quad (2)$$

As shown in Fig. 3(a), the cartridge uses an outer and an inner mesh of 40 mm in length, which are 62 mm and 40 mm in diameter, respectively. These meshes are stainless steel braided with pores about 2–3 μm and thickness about 80 μm . The thickness and pores ensure that the gas conductance through the particle bed prevails over any leak at the attachment points. Both of the meshes are supported by homocentric frames. One end of the frames is attached to the shaft of the rotary manipulator, while the other end is supported by a bearing on the cavity cover to alleviate radial vibration. The outer mesh acts as the gas distributor while the inner one takes the role of particle filter. In operation, flexible adjustment of fluidization is controlled by rotation speed and fluidizing gas velocity. The cartridge rotates under the drive of the shaft and particles are evenly distributed on the gas distributor, forming an annular bed. As Fig. 3(b) shows, when the fluidizing gas flows into the cartridge radially, drag force acts on particle bed in the opposite direction to the centrifugal force. With the gas velocity increasing, uniform fluidization is finally reached when the centrifugal force is balanced by the gas drag force.

D. Rotary manipulator components

Rotary motion of particle cartridge is provided by rotary manipulator components, including a stepper motor, a coupling, a rotary feedthrough, and a customized cross flange. The stepper motor with a maximum rotating speed of 1200 rpm is precisely controlled by closed-loop negative feedback. The minimum rotation speed to form an annular particle bed in the cartridge is $n_0 = 42.4/(2r_0)^{0.5}$ given by Suarez,³⁹ which is 172 rpm in our cartridge. Therefore, the motor usually works at rotation speed higher than 180 rpm for ALD reactions, creating centrifugal force larger than 1.12 times of gravity. A magnetic fluid feedthrough is used as the rotary feedthrough, and its magnets allow all the fluidizing gas and precursors flow exclusively through the meshes on the cartridge. Water cooling is necessary to keep the temperature

of the magnets below 110 °C to prevent losing magnetism. The customized cross flange acts as a joint shell between the magnetic fluid feedthrough and the motor. Rotation is transmitted from the motor to the feedthrough by a magnetic coupling which satisfies vacuum requirement.

E. Pumping section

Vacuum is maintained by a double-acting vane pump from Edwards Vacuum® RV12. As shown in Fig. 1, two parallel pumping bypasses are configured with the first one for initial evacuation before deposition, and the second one for maintaining vacuum during deposition. In the pumping down stage, particles tend to clog the pores of the inner mesh because of large gas turbulence. To solve this problem, stepped pumping is conducted using a manual throttle valve and a fast closing gate valve on the first bypass. By repeating the micro-open/close sequence (70–100 ms/2 s) hundreds of times, the pressure of the chamber decreases to vacuum, while the turbulence could be reduced effectively by extending the pumpdown time. The throttle valve first allows a small gas flow and then gradually opens wider to further smooth the gas flow. Small gas turbulence during each step reduces particle loss to less than 3%, while no particles are observed to clog mesh pores after they are taken out from the cartridge. When the chamber pressure decreases to vacuum level, the first pumping bypass is closed and the second one begins to control reactor pressure. The waste corrosive chemicals are first decomposed through a tube furnace and then be eliminated by flowing through a filter before entering the pump.

III. EXPERIMENT SECTION

Fluidization and coating experiments were conducted under different superficial gas velocities and rotation speeds. In the particle cartridge, 10 g spherical silicon oxide NPs (Aladdin® M120353) of 250–300 nm were held, with the surface area of 10.12 m²/g measured by Brunner-Emmet-Tellet (BET) measurements. High purity N₂ (99.999%) acted as the fluidizing gas, and thin Al₂O₃ shells were deposited on the surfaces using trimethyl-aluminum (TMA) and H₂O (ultrapure, MilliQ) as precursors. Before deposition, these particles were dried under vacuum (0.1 Torr, 100 °C) for at least 2 h. The operating temperature at 180 °C inside the chamber was achieved before deposition and kept stable during the whole process.

A. Stable fluidization of rotating particles

Obtaining a stable fluidization is the first step to achieve optimal coating process. The gas channels, slugs, and the motion of the bed surface with time have strong influences on pressure fluctuation. As a result, the pressure fluctuation is widely used to monitor the hydrodynamics and stability of a fluidized bed. The background pressure drop was measured without particles in the cartridge, which was then subtracted from the pressure drop for the cartridge with 10 g particles. We used 180 rpm, 300 rpm, and 420 rpm as representatives of low, mediate, and high rotation speeds, respectively. Since 10 g

particles occupied an apparent volume of 13 cm³ according to our test and the density of the SiO₂ was 2.32 g/cm³, the bed void fraction ε was about 0.7. At 180 rpm rotation speed, the acceleration is close to gravitational one; thus, the bed void fraction is supposed to be 0.7 when there is no fluidizing gas. Considering the size of the particle cartridge, the radius of inner particle bed surface r_i is 29.3 mm and the apparent weight of the particles per unit area is 12.6 N. Therefore, when fluidization is added, the gas pressure drop across the particle bed at 180 rpm is equal to the apparent weight of the particles per unit area, which is estimated as 12.6 Pa. Given the fluidizing gas density of 1.36 g/l and the stable pressure drop to be in proportion to ω^2 as Equation (2) shows, the theoretical stable pressure drop under 180 rpm, 300 rpm, and 420 rpm during fluidization was 12.6 Pa, 35.0 Pa, and 68.6 Pa, respectively.

Rotation speed is important in facilitating fluidizing uniformity and stability of nanoparticles. As shown in Fig. 4(a), the pressure drop increased with the superficial gas velocity growing, accompanied with enlarged interstitials. The pressure drop finally reached a plateau when exceeded the minimum fluidizing velocity. Under a rotation speed of 180 rpm, the pressure drop fluctuation was quite obvious. Elimination of gas channels or slugs in particle bed was ineffective due to the lack of strong interactions between gas and particles. When rotation speed increased to 300 rpm, the pressure drop stabilized at the superficial gas velocity of 6 cm/s. Compared with 180 rpm, the higher rotation speed provided larger centrifugal force to overcome the cohesive

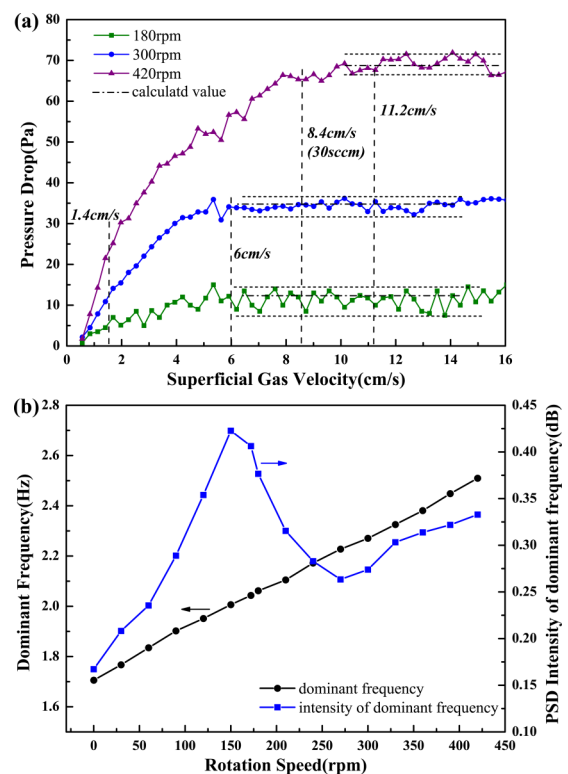


FIG. 4. (a) Pressure drop across the nanoparticle bed under different superficial gas velocities and rotation speeds and (b) dominant frequency and intensity of pressure drop fluctuation PSD under various rotation speeds with 8.4 cm/s fluidizing gas.

force. The gas-solid interaction was sufficiently facilitated to eliminate gas channels and slugs, leading to much more uniform and stable fluidization. Continuing the increase of the rotation speed to 420 rpm exerted larger centrifugal force with little pressure drop fluctuation. It should be noted that minimum fluidizing velocity as high as 11.2 cm/s was required at 420 rpm. Considering those precursors with relatively low reaction sticking coefficient may leave the particle bed directly without reaction; excessive fluidizing gas velocity might be inappropriate in practical operations.

The oscillation frequency and intensity of the pressure fluctuation in the fluidized bed are analyzed by PSD.^{40,41} Under 8.4 cm/s fluidizing velocity, the pressure drop at different rotation speeds was recorded and processed by auto-correlation and Fast Fourier Transform (FFT). Differentiation of the various fluidization stabilities is thereafter achieved by observing the dominant frequency and intensity as shown in Fig. 4(b). The dominant frequency of pressure drop oscillation increased with rotation speed, indicating the periodicity of fluctuations becomes weaker. The intensity of each dominant frequency increased initially, since more fluidizing gas went through the particle bed and made the fluctuation apparent. The maximum intensity appeared when the minimal rotation speed to form annular particle bed was reached (172 rpm). Continuing the increase of the rotation speed to 270 rpm would help eliminate gas channels or slugs; thus, the intensity of spectrum decreased. This is consistent with the pressure drop fluctuation at 300 rpm shown in Fig. 4(a) which confirms a stable fluidization. Rotation speed larger than 300 rpm showed a slight increase of PSD intensity due to excess collisions and frictions between particles and the gas distributor or particles themselves. From the analysis above, if choosing 8.4 cm/s fluidizing gas, the optimized rotation speed ranges from 240 rpm to 320 rpm, providing a stable fluidized rotating bed for ALD on particles.

B. Alumina ALD growth

The growth linearity is an important factor for ALD process, and different ALD cycles were conducted under optimal conditions (8.4 cm/s superficial gas velocity and 300 rpm rotation speed). Quantitative analysis was performed by Inductively Coupled Plasma-Optical Emission Spectroscopy (ICP-OES). The mass concentration of aluminum was used to calculate the thickness of coated shell, which was the mass content of Al in the whole synthesized core-shell SiO₂@Al₂O₃ nanoparticles. In operation, a strong NaOH solution was used to dissolve the coated films from the particles, while the SiO₂ particle itself would not dissolve. As shown in Fig. 5, the Al mass concentration has a nearly linear relationship with coating cycle which was less than 100, and then its increasing rate would gradually slow down since more alumina has been coated whose weight compared with that of the original particle could not be ignored especially when hundreds of cycles have been completed. Given the density of alumina films about 3 g/cm³ at 180 °C, the calculated Al₂O₃ ALD growth rate increased from 0.82 Å/cycle to 1.01 Å/cycle, corresponding to deposition cycles increased from 11 to 800, close to reported data.⁴² The discrepancy between such growth

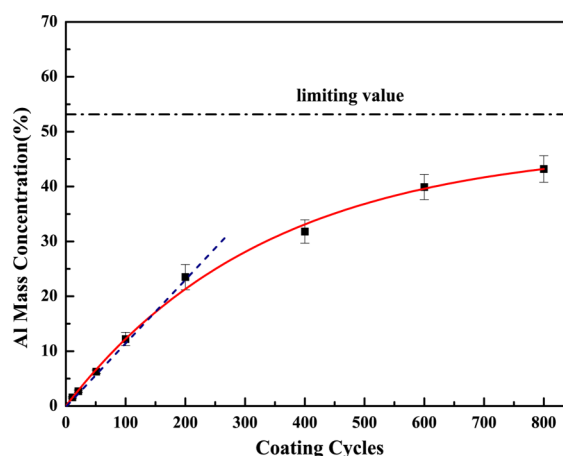


FIG. 5. ICP-OES Al mass concentration as a function of coating cycle numbers.

rates is probably ascribable to the number of cycles. The initial growth might be inhibited by the SiO₂ particles' surface chemistry, and after a certain of deposition cycles, the growth reached a steady state as the surface turn to alumina.

C. ALD cycle time reduction

NPs have very large specific surface area that is several orders of magnitude that of planar substrates'; thus, a reduced cycle time for saturated ALD growth is crucial for practical applications. The stable and homogeneous fluidization of particle bed would improve the diffusion of precursors which helps shorten the cycle time. To simplify the experiment procedure, 11 cycles coating was chosen for quantitative analysis with different pulse times of 2 sccm TMA/H₂O.

Superficial gas velocities of 1.4 cm/s and 8.4 cm/s were used to compare the coating efficiency. Based on the former fluidization experiments, 8.4 cm/s gas flow was sufficient to get a fully fluidized and stabilized rotary particle bed under 300 rpm rotation speed. In contrast, 1.4 cm/s fluidizing gas had little effect on dispersing particles, which behaved like single-rotation acting reactors especially when the rotation speed

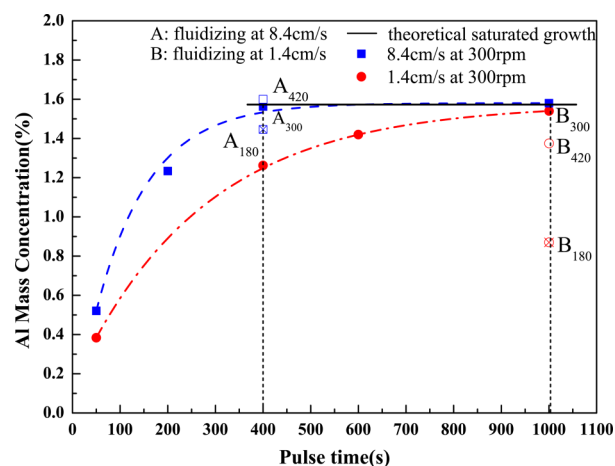


FIG. 6. ICP-OES Al content measured as a function of the pulse time with different fluidizing and rotating parameters.

further decreased. Al mass concentration fitting curves of both velocities in Fig. 6 finally saturated close to the theoretical value, meaning a complete coating on all particle surfaces. It cost 1000 s to get saturation for 1.4 cm/s gas velocity, while the curve representing 8.4 cm/s ascended faster with the minimum pulse time reduced to 400 s. When the superficial gas velocity was as low as 1.4 cm/s, the rotating particle bed was not fluidized well. The particle bed was almost fixed and the interstitials stayed narrow and nonuniform. Though precursors flew into the annular particle bed uniformly through the gas distributor, their diffusion inside the bed was hindered and thus longer pulse time was needed to get complete coating. When fluidizing velocity increased to 8.4 cm/s, the rotating particle bed had been sufficiently fluidized. Precursor diffusion was facilitated; thus, the minimum pulse time for saturation was reduced.

Rotation speed also affects the deposition rate throughout the entire particle bed. At 180 rpm rotation speed, like conventional fluidized bed, the existence of gas channels or slugs led to some precursors flowing through these bypasses directly without participating in reactions, leading to lower Al mass concentrations (points A₁₈₀ and B₁₈₀) compared with 300 rpm. Using 420 rpm, however, the growth rate (point A₄₂₀) was much more close to that of 300 rpm, though a little lower coating speed at 1.4 cm/s (point B₄₂₀) was attributed to the incapability of sufficiently fluidizing particle bed. By optimizing the superficial gas velocity, expedite diffusion of precursor in the particle bed is obtained which is assisted by sufficient rotation speed.

D. Precursor utilization

Compared to flat surface ALD process, large surface area of NPs requires significant amount of precursors. The economic feasibility strongly depends on the precursor efficiency as mentioned by Grillo *et al.*⁴³ Therefore, it is important to design reactor and processes with enhanced precursor usage during coating. The precursor usage in a half-reaction can be evaluated by the percentage of the cumulative by-product before any unreacted precursor leaving the particle bed in all the by-product. An AMETEK® quadrupole mass spectrometer (QMS) was used to detect the partial pressure of each gas, using molecule sampling components that connect the needle valve of the mass spectrometer directly with the chamber outlet. A 6 Torr molecular microporous 1/4 in. Vacuum Coupling Radius (VCR) seal gasket is fixed on the needle valve to protect the filament of QMS. The needle valve and the pipes between it and the quadrupole are wrapped by heating resistance collar and the temperature is maintained at 150 °C to fasten the desorption of molecules that were absorbed on the surfaces of stainless steel. In Al₂O₃ ALD using TMA and H₂O as precursors, the expected by-product is CH₄. However, in a TMA half-reaction, CH₄ is also generated from the fragmentation of TMA in the mass spectrometer. To solve this problem, H₂O was replaced by D₂O to trace the amount of ALD by-product methane from the total signal of methane. The detected *m/z* peaks for D₂O and CH₃D were 20 and 17. In order to detect the TMA signal, the signal amplifier was turned on to obtain three orders of magnitude higher for all signals.

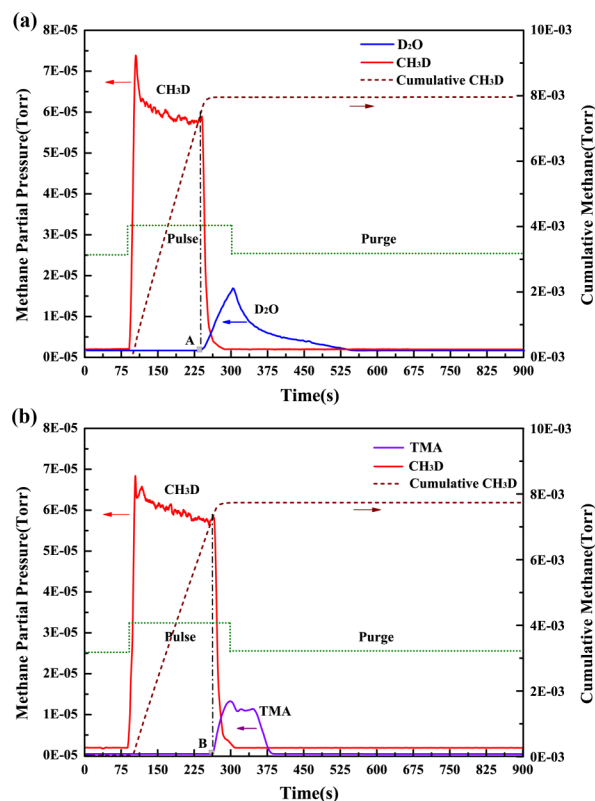


FIG. 7. *In situ* mass spectrometry results of (a) D₂O half-reaction and (b) TMA half-reaction.

Precursor pulses of 4 sccm were given, accompanied with 300 rpm rotation speed and 8.4 cm/s fluidizing gas. Data sampling frequency was 15 ms and smoothing was performed using Savitzky-Golay method to eliminate irregular and noisy data.

As illustrated in Fig. 7(a), a 220 s pulse time was provided for D₂O precursor when sufficient TMA precursor had already been injected and purged for 2-3 min. Once the D₂O pulse began, the partial pressure of reaction by-product CH₃D had an instantaneous increase and kept at a certain stage for about 200 s. Then, the signal of CH₃D decreased rapidly as the dose proceeding, which made a stepwise profile. No CH₃D was detected after this stage, suggesting no residue of reactive sites in the particle bed. D₂O signal did not increase until methane decreased to point A near its base line and it decreased slowly because of its viscosity. The aforementioned tendency shows that almost all the D₂O had participated in the half-reaction before coatings on all particles were complete. By integrating the produced CH₃D, the cumulative CH₃D curve during this half-reaction was obtained which increased with pulse time initially, and then leveled out after the reaction had been saturated. Prior to point A where D₂O signal began to increase, about 93% of the cumulative methane had been generated. To validate the above quantitative analysis by mass spectroscopy, precursor weighting experiment was performed. The consumed water was 11 mg in 200 s, while using the BET surface area of 10.12 m²/g, 11.7 mg D₂O is needed for complete coating on 10 g particles in calculation. Thus, the consumption by QMS analysis was in a good agreement with the calculation. Similar trends of TMA half-reaction were observed as Fig. 7(b) shows, and the utilization of TMA was nearly 90%.

For rotary reactors which do not couple radial fluidization, low speed rotary agitation and long exposure time have been utilized.^{22,44} For a total surface area of 15.2 m², the half reaction including static exposure stage costs ~65 s to make the most of precursors.⁴⁴ Since the saturated reaction time and the total surface area have a linear relationship,²² about 433 s would be needed to coat the same surface area as 10 g particles had in our experiment. For fluidization coupled rotary reactor discussed here, the half reaction time could be shortened to half of it, mainly due to that particles could be dispersed and exposed to precursors simultaneously under high speed rotation. The particle bed interstitials were enlarged and homogeneous, ensuring the uniform diffusion of precursors inside the bed. The pulse duration could be further reduced by optimizing fluidizing velocity and rotation speed with larger precursor flow. The design of fluidization coupled rotary reactor ensures high precursor usage along with faster ALD cycles and will be quite attractive for a lot of practical usage.

E. Microstructure characterizations of coated shells

Besides former macroscopic statistical average of deposition rate, the microstructure of individual particle was studied by High Angle Annular Dark Field-Transmission Electron Microscopy (HAADF-TEM). Fig. 8(a) shows the HRTEM image in bright field of 200 ALD cycles Al₂O₃ coated SiO₂ NPs. Distinct Al₂O₃ film on the outside edge of each individual particle suggested the coating to be conformal and smooth. From Energy Dispersive X-ray (EDX) spectroscopy line scans in Fig. 8(c), Al, O, and Si signals were detected. At the point where the arrows crossed the edges of the particles, clear peak

in Al signal and steep decrease in Si signal were observed. The results indicated that the particle consisted of a SiO₂ core surrounded by a 16.4 nm thick Al₂O₃ shell. For generosity check, CeO₂ nanopolyhedras synthesized based on instructions reported by Mai *et al.*⁴⁵ were also coated with 100 cycles Al₂O₃. The HAADF-TEM image in Fig. 8(b) confirmed that all particles had been homogeneously coated, and the EDX line scan in Fig. 8(d) showed a film thickness about 8.6 nm. Above all, the growth rate was 0.8–0.9 Å/cycle based on the TEM and line scan results, which is consistent with the calculated value by ICP-OES. Combined with microscopic characterization, we conclude that uniform and controllable films can be deposited on nanoparticles, irrespective of particle sizes and shapes.

IV. CONCLUSION

In this article, a rotary ALD reactor coupled with fluidization is introduced for atomic layer coating on NPs. The cylindrical particle cartridge uses fluidization to disperse particles, and it adopts high speed rotation to enhance gas-solid interactions for uniform and stable fluidization of particle bed, which was demonstrated by experimental pressure drop and related power spectrum density analysis. The enlarged particle bed interstitials and enhanced gas-solid interactions facilitate precursor transport throughout the particle bed and reduce the minimum cycle time. The cartridge ensures precursors' flow exclusively through the particle bed to achieve high precursor utilization needless of static exposure, confirmed by *in situ* mass spectrometry results of each half-reaction. ICP-OES, HAADF-TEM, and EDX results of Al₂O₃ shells on SiO₂ and CeO₂ nanoparticles confirmed the controllability and uniformity of deposition, as well as the generosity on various nanostructures. The reactor provides an effective approach for particle ALD with both high reactant usage and accelerated process.

ACKNOWLEDGMENTS

The authors would like to thank Deng Zhang and Kun Cao for insightful discussion, technology supports by the Analytic Testing Center of HUST for carrying out HAADF-TEM and EDX analysis, National Engineering Research Center for Nanomedicine for BET test, Materials Research and Test Center of WUT for ICP measurement, and Ao-Ming Li from AMETEK Lab for *in situ* spectrometry. This work is supported by the National Basic Research Program of China (No. 2013CB934800), the Hubei Province Funds for Distinguished Young Scientists (Nos. 2015CFA034 and 2014CFA018), the State Key Laboratory of Digital Manufacturing Equipment and Technology Funding (No. DMET2015A01), the Fundamental Research Funds for the Central Universities, HUST (No. 2014TS037), as well as the Program for Changjiang Scholars and Innovative Research Team in University (No. IRT13017). Rong Chen acknowledges the Thousand Young Talents Plan and the Recruitment Program of Global Experts.

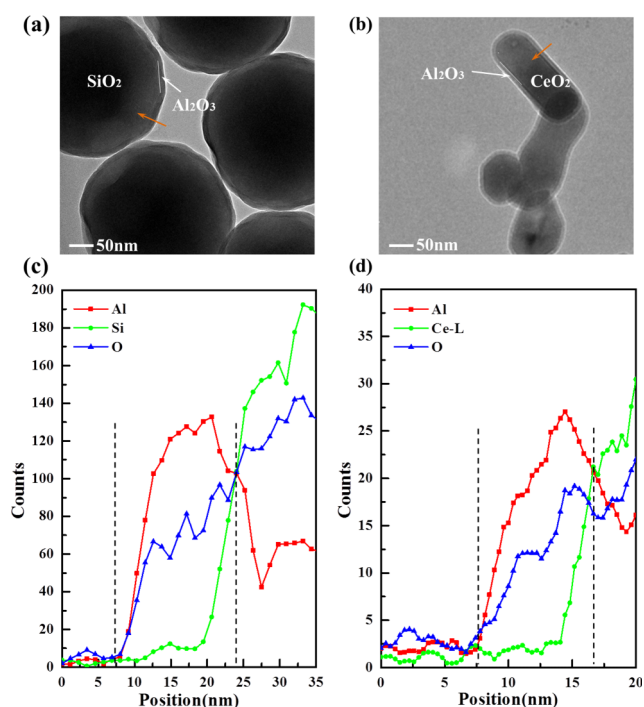


FIG. 8. HRTEM images of (a) 200 cycles Al₂O₃ coating on SiO₂ nanoparticles, (b) 100 cycles Al₂O₃ coating on CeO₂ nanopolyhedras and EDX line scans of (c) 200 cycles Al₂O₃ coating on SiO₂ nanoparticles, and (d) 100 cycles Al₂O₃ coating on CeO₂ nanopolyhedras.

¹P. Vashishta, R. K. Kalia, and A. Nakano, *J. Phys. Chem. B* **110**, 3727 (2006).

²A. Yanguas-Gil and J. W. Elam, *J. Vac. Sci. Technol., A* **32**, 031504 (2014).

³M. Ozawa, *J. Alloys compd* **408**, 1090 (2006).

- ⁴Z. Ma, S. Brown, J. Y. Howe, S. H. Overbury, and S. Dai, *J. Phys. Chem. C* **112**(25), 9448 (2008).
- ⁵N. Ihara, H. Kodama, and T. Uzumaki, U.S. patent 20050260340 (24 November 2005).
- ⁶C. Marichy, M. Bechelany, and N. Pinna, *Adv. Mater.* **24**, 1017 (2012).
- ⁷S. Chervinskii, A. Matikainen, A. Dergachev, A. A. Lipovskii, and S. Honkanen, *Nanoscale Res. Lett.* **9**, 398 (2014).
- ⁸X. Lin, K. H. Yu, G. H. Lu, J. H. Chen, and C. Yuan, *J. Phys. D: Appl. Phys.* **46**, 024004 (2013).
- ⁹S. A. Skoog, J. W. Elam, and R. J. Narayan, *Int. Mater. Rev.* **58**, 113 (2013).
- ¹⁰V. P. Shastri, I. Chen, W. Znidarsic, W. Znidarsic, and I. W. Chen, W.O. patent 2004085998 (28 March 2003).
- ¹¹Y. Horiguchi, T. Kanda, K. Torigoe, H. Sakai, and M. Abe, *Langmuir* **30**, 922 (2014).
- ¹²S. Xie, S.-I. Choi, N. Lu, L. T. Roling, J. A. Herron, L. Zhang, J. Park, J. Wang, M. J. Kim, Z. Xie, M. Mavrikakis, and Y. Xia, *Nano Lett.* **14**, 3570 (2014).
- ¹³M. Coskun and M. Korkmaz, *J. Nanopart. Res.* **16**, 2316 (2014).
- ¹⁴M.-l. Yuan, J.-h. Tao, G.-j. Yan, M.-y. Tan, and G.-z. Qiu, *Trans. Nonferrous Met. Soc. China* **20**, 632 (2010).
- ¹⁵L. F. Hakim, J. H. Blackson, and A. W. Weimer, *Chem. Eng. Sci.* **62**, 6199 (2007).
- ¹⁶M. Knez, K. Niesch, and L. Niinistö, *Adv. Mater.* **19**, 3425 (2007).
- ¹⁷S. M. George, *Chem. Rev.* **110**, 111 (2010).
- ¹⁸T. Tynell and M. Karppinen, *Semicond. Sci. Technol.* **29**, 043001 (2014).
- ¹⁹D. Longrie, D. Deduytsche, and C. Detavernier, *J. Vac. Sci. Technol., A* **32**, 183 (2014).
- ²⁰J. A. McCormick, K. P. Rice, D. F. Paul, A. W. Weimer, and S. M. George, *Chem. Vap. Deposition* **13**, 491 (2007).
- ²¹J. D. Ferguson, A. W. Weimer, and S. M. George, *Thin Solid Films* **371**, 95 (2000).
- ²²D. Longrie, D. Deduytsche, J. Haemers, K. Driesen, and C. Detavernier, *Surf. Coat. Technol.* **213**, 183 (2012).
- ²³A. S. Cavanagh, C. A. Wilson, A. W. Weimer, and S. M. George, *Nanotechnology* **20**, 255602 (2009).
- ²⁴X. H. Liang, G. D. Zhan, D. M. King, J. A. McCormick, J. Zhang, S. M. George, and A. W. Weimer, *Diamond Relat. Mater.* **17**, 185 (2008).
- ²⁵J. H. Li, X. H. Liang, D. M. King, Y. B. Jiang, and A. W. Weimer, *Appl. Catal., B* **97**, 220 (2010).
- ²⁶J. R. Wank, S. M. George, and A. W. Weimer, *J. Am. Ceram. Soc.* **87**, 762 (2004).
- ²⁷J. R. Wank, S. M. George, and A. W. Weimer, *Powder Technol.* **142**, 59 (2004).
- ²⁸X. H. Liang, K. S. Barrett, Y. B. Jiang, and A. W. Weimer, *ACS Appl. Mater. Interfaces* **2**, 2248 (2010).
- ²⁹L. F. Hakim, S. M. George, and A. W. Weimer, *Nanotechnology* **16**, S375 (2005).
- ³⁰D. M. King, J. A. Spencer, X. Liang, L. F. Hakim, and A. W. Weimer, *Surf. Coat. Technol.* **201**, 9163 (2007).
- ³¹D. M. King, X. H. Liang, Y. Zhou, C. S. Carney, L. F. Hakim, P. Li, and A. W. Weimer, *Powder Technol.* **183**, 356 (2008).
- ³²D. Longrie, D. Deduytsche, J. Haemers, P. F. Smet, K. Driesen, and C. Detavernier, *ACS Appl. Mater. Interfaces* **6**, 7316 (2014).
- ³³A. P. Didden, J. Middelkoop, W. F. A. Besling, D. E. Nanu, and R. van de Krol, *Rev. Sci. Instrum.* **85**, 013905 (2014).
- ³⁴L. F. Hakim, J. L. Portman, M. D. Casper, and A. W. Weimer, *Powder Technol.* **160**, 149 (2005).
- ³⁵C. Zhu, Q. Yu, R. N. Dave, and R. Pfeffer, *AIChE J.* **51**, 426 (2005).
- ³⁶J. R. van Ommen, J. M. Valverde, and R. Pfeffer, *J. Nanopart. Res.* **14**, 737 (2012).
- ³⁷J. M. Valverde, M. A. S. Quintanilla, A. Castellanos, D. Lepek, J. Quevedo, R. N. Dave, and R. Pfeffer, *AIChE J.* **54**, 86 (2008).
- ³⁸T. J. Larrabee, T. E. Mallouk, and D. L. Allara, *Rev. Sci. Instrum.* **84**(1), 014102 (2013).
- ³⁹C. E. Suarez, *Light Metals 2012* (Wiley-TMS, New Jersey, 2012).
- ⁴⁰M. F. Llop and N. Jand, *Chem. Eng. J.* **95**, 25 (2003).
- ⁴¹R. C. Brown and E. Brue, *Powder Technol.* **119**, 68 (2001).
- ⁴²R. L. Puurunen, *J. Appl. Phys.* **97**(12), 121301 (2005).
- ⁴³F. Grillo, M. T. Kreutzer, and J. R. van Ommen, *Chem. Eng. J.* **268**, 384 (2015).
- ⁴⁴J. A. McCormick, B. L. Cloutier, A. W. Weimer, and S. M. George, *J. Vac. Sci. Technol., A* **25**(1), 67 (2007).
- ⁴⁵H. X. Mai, L. D. Sun, Y. W. Zhang, R. Si, W. Feng, H. P. Zhang, H. C. Liu, and C. H. Yan, *J. Phys. Chem. B* **109**, 24380 (2005).